machines

MDPI

Article

Suction Performance Optimization of a Grease Suction and Discharge Device for Wind Turbine Bearings Considering Herschel–Bulkley

Han Peng [1,2,*], Budi Peng [1], Linjian Shangguan [1,*], Mingxuan Zhang [1], Minzhang Zhao [3], Lei Liu [1], Zihao Qin [1], Zihao Meng [1], Yihao Zhang [1] and Bingli Huang [3]

[1] School of Mechanical Engineering, North China University of Water Resources and Electric Power, Zhengzhou 450045, China; pbd286500@163.com (B.P.); 18039273752@163.com (M.Z.); liulei@ncwu.edu.cn (L.L.); 15737882156@163.com (Z.Q.); mzh000311@163.com (Z.M.); 18539131830@163.com (Y.Z.)

[2] School of Water Conservancy, North China University of Water Resources and Electric Power, Zhengzhou 450045, China

[3] Zhengzhou Autol Technology Co., Ltd., Zhengzhou 450011, China; zmz@autol.net (M.Z.); hbl@autol.net (B.H.)

* Correspondence: penghan@ncwu.edu.cn (H.P.); shangguanlinjian@ncwu.edu.cn (L.S.); Tel.: +86-158-3831-9395 (H.P.)

Abstract

With the advancement of industrial IoT and artificial intelligence technologies, bearing maintenance is gradually evolving toward predictive maintenance. For large bearings, the internal grease must be replaced promptly once it has deteriorated. As the core lubrication component of such bearings, the suction and discharge device directly determines the efficiency of grease discharge and the operational stability of the bearing. To address the issue of insufficient intake capacity in existing units, this study employs the Herschel–Bulkley non-Newtonian fluid model to analyze intake characteristics and conduct multi-parameter co-optimization, revealing the underlying mechanisms by which vacuum level, grease temperature, and the chamfer structure of the grease inlet pipe influence suction performance. Based on the yield stress and shear thinning characteristics of the grease, the flow equation for the inlet section was derived, and the analytical and CFD results showed consistent trends. With the volumetric flow rate in the inlet section as the optimization objective, a multi-parameter co-optimization of the vacuum level, temperature, and chamfer radius was conducted through orthogonal experiments. The results show that under the optimal parameter combination, the inlet volumetric flow rate was significantly increased, and grease supply stability was markedly improved. The research findings provide a theoretical basis and engineering reference for the design optimization of the suction and discharge device for wind turbine bearings.

Keywords: suction and discharge device; inhalation characteristics; orthogonal optimization; Herschel–Bulkley model

Check for updates

Academic Editor: Hongrui Cao

Received: 8 July 2026
Revised: 4 August 2026
Accepted: 5 August 2026
Published: 7 August 2026

Copyright: © 2026 by the authors. Licensee MDPI, Basel, Switzerland. This article is an open access article distributed under the terms and conditions of the Creative Commons Attribution (CC BY) license.

1. Introduction

In mechanical equipment, large bearings, especially those used in wind turbines and other heavy-duty machinery, are difficult to disassemble and maintain [1]. Once the grease inside the bearing becomes aged, contaminated, or excessively hardened, timely

replacement is critical to prevent lubrication failure and bearing damage [2]. In centralized lubrication and grease-recovery systems, the suction–discharge device serves as a key actuator for removing aged grease and ensuring continuous grease replacement. Its suction performance directly affects waste-grease extraction efficiency and bearing-system stability. Among various application fields, wind turbines impose particularly demanding requirements on bearing lubrication reliability because they operate for long periods under variable loads, low temperatures, vibration, and complex environmental conditions [3,4]. Compared with traditional manual grease injection, centralized lubrication systems can reduce shutdown time, manual tower-climbing operations, and delayed relubrication, thereby improving the continuity and safety of bearing maintenance [5].

In practical operation, insufficient suction is a major limitation of grease suction–discharge devices, particularly when aged or low-temperature grease must pass through a compact inlet channel [6,7]. Existing designs are commonly based on empirical adjustments or single-factor analyses and therefore cannot adequately describe the coupled influence of operating conditions and inlet geometry [8]. A systematic investigation is thus required to identify the key factors governing suction performance and determine an effective parameter combination.

Previous studies relevant to the present work can be broadly grouped into four areas: grease degradation, non-Newtonian flow and lubrication modeling, transient pipe-flow and hydraulic-wave phenomena, and the design of waste-grease recovery devices. Zhang et al. [9] investigated grease aging under hot-air conditions and reported that base-grease separation and thickener deterioration are important causes of grease degradation. Li [10] analyzed the evolution of soap-fiber structures during thermal aging and showed that temperature variation can alter the degree of fiber entanglement. Zhao [11] further studied the thermal-aging mechanism of lithium-based grease and found that prolonged thermal exposure may cause thickener-fiber fracture, aggregation, hardening, base-grease oxidation, and evaporation. These studies indicate that temperature and aging can significantly change the structural stability and flow resistance of grease, which provides an important basis for analyzing grease suction performance.

From a fluid-mechanics perspective, lubricating grease can be regarded as a viscoplastic non-Newtonian material with yield stress and shear-thinning behavior. Yusufi et al. [12] reviewed recent advances in modeling Herschel–Bulkley fluids in pipes and summarized theoretical, empirical, computational, and experimental approaches for pressure-driven flow prediction. Calusi et al. [13] investigated viscoplastic flows in narrow channels and showed that channel geometry and model regularization can affect the predicted flow field. In the field of bearing lubrication, Maccioni and Concli [14] reviewed CFD approaches for lubricated mechanical components, including gears, bearings, and pumps, and summarized numerical strategies for simulating lubricant flow and component-level lubrication behavior. Obata et al. [15] studied the effect of grease viscosity on the channeling properties of ball bearings and showed that grease flow behavior is closely related to viscosity characteristics and bearing geometry. In addition, van der Meer and Van Ostayen [16] developed a solution method for the Reynolds equation with Herschel–Bulkley fluids, showing the continued relevance of H-B rheology in lubrication modeling.

Beyond steady pressure-driven pipe flow, the suction stroke of a plunger-type device is inherently transient because plunger motion continuously changes the working-chamber volume, pressure, and inlet flow rate. Stosiak et al. [17] showed that pulsating pump output may generate pressure-wave amplification in hydraulic pipelines, whereas Urbanowicz et al. [18] demonstrated that accelerating pipe flow exhibits velocity-profile development that differs from steady flow. These studies indicate that transient acceleration and pressure variations may affect flow start-up. However, they mainly concern Newtonian fluids,

idealized pipelines, or relatively long hydraulic transmission lines. The suction behavior of viscoplastic grease in the short and chamfered inlet channel of a grease suction–discharge device therefore remains insufficiently quantified.

At the system and device levels, Li [19] developed a waste-grease recovery and regeneration system based on circulating filtration. Chen [20] analyzed the reasons why used grease cannot enter the grease collection bottle and proposed an improvement scheme for the grease recovery process. Quan [21] designed a centralized recovery system for bearing waste grease and grinding debris. Si [22] introduced a grease-quality sensor between the suction–discharge device and the waste-grease tank to evaluate the quality of discharged grease. Suo [23] developed a rotary suction–discharge device to simplify the layout of multi-point grease discharge systems and improve discharge efficiency. These studies improve the automation, monitoring, and structural arrangement of grease recovery systems. Nevertheless, most of them focus on system-level design or recovery-device configuration, whereas the internal suction-flow mechanism of the suction–discharge actuator remains insufficiently quantified.

Accordingly, the novelty of the present study lies in integrating experimentally measured grease rheology, an analytical Herschel–Bulkley pipe-flow model, CFD simulations, and multi-parameter orthogonal optimization. Unlike previous studies that separately addressed grease rheology, idealized non-Newtonian flow, or waste-grease recovery system design, this work quantitatively evaluates the coupled effects of vacuum level, grease temperature, and inlet chamfer radius on the suction performance of a short-channel grease suction–discharge device. The main objectives are: (1) to determine the Herschel–Bulkley parameters of the selected grease at different temperatures; (2) to establish an analytical and numerical model of the inlet suction process; (3) to clarify the effects of vacuum level, grease temperature, and chamfer radius on the inlet flow field; and (4) to determine an optimized parameter combination for improving suction capacity and flow stability.

2. Structural Simplification and Suction-Flow Analysis of the Grease Suction and Discharge Device

2.1. Operating Principle and Simplified Flow Domain

The grease suction–discharge device is a key actuator in the waste-grease recovery system of large bearing lubrication equipment. Its main function is to generate a pressure difference during the suction stroke, draw aged grease from the bearing outlet into the working chamber, and then discharge the collected grease to the recovery line during the discharge stroke. Therefore, the device determines whether aged or hardened grease can be continuously removed from the bearing housing. A schematic diagram of the used grease recovery system is shown in Figure 1.

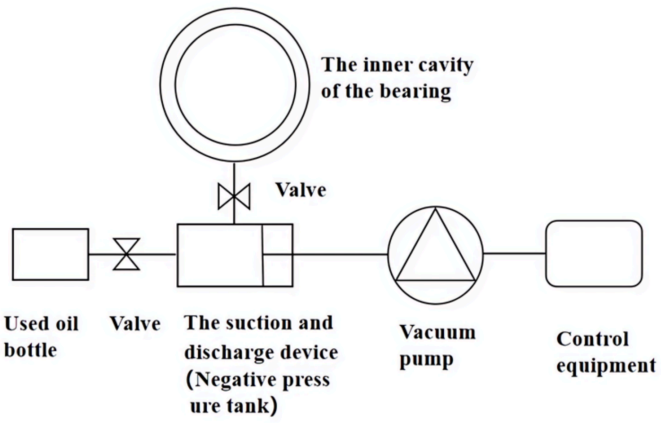


Figure 1. Structural principles of a waste grease recovery system.

The operating cycle of the grease suction–discharge device consists of two stages: the suction stroke and the discharge stroke. During the suction stroke, the plunger moves backward, increasing the volume of the working chamber and reducing the chamber pressure. Under the pressure difference between the bearing outlet and the working chamber, grease enters the chamber through the inlet channel. During the discharge stroke, the plunger moves forward, decreasing the chamber volume and forcing the grease out through the discharge channel. The schematic structure of the grease suction–discharge device is shown in Figure 2.

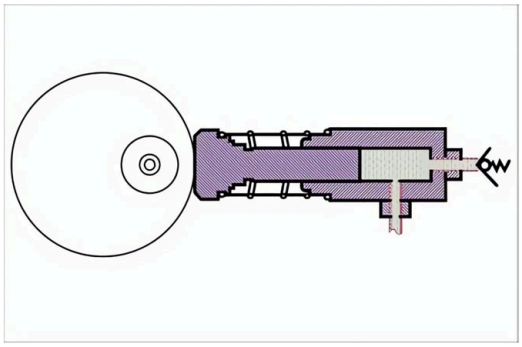


Figure 2. Schematic diagram of the suction and discharge device.

Compared with the discharge stroke, the suction stroke is more easily affected by the rheological properties of grease and the local resistance of the inlet channel. Before entering the working chamber, grease must overcome its yield stress and the pressure loss caused by the short and narrow inlet passage. Insufficient suction may lead to incomplete chamber filling, reduced volumetric efficiency, and unstable waste-grease extraction. Therefore, this study focuses on the suction stroke of the grease suction–discharge device, while the discharge process is not analyzed in detail [24–28].

During the actual suction stroke, the backward motion of the plunger continuously increases the working-chamber volume and reduces the chamber pressure. Consequently, the grease accelerates from its initial state and the inlet flow rate varies with time before approaching a relatively stable condition. The actual suction process is therefore transient in nature. However, to establish a tractable analytical relationship between the pressure gradient, grease rheological parameters, and inlet flow rate, the inlet channel is analyzed using an idealized steady and fully developed pipe-flow model.

For the subsequent flow analysis, the actual device was simplified by retaining only the regions directly involved in grease transport. The inlet channel, working chamber, and discharge channel were preserved, whereas non-flow structures, including threads, mounting holes, external fittings, and support components, were omitted. This simplification reduces geometric complexity while retaining the primary flow path governing suction performance. The resulting simplified flow-domain model is shown in Figure 3.

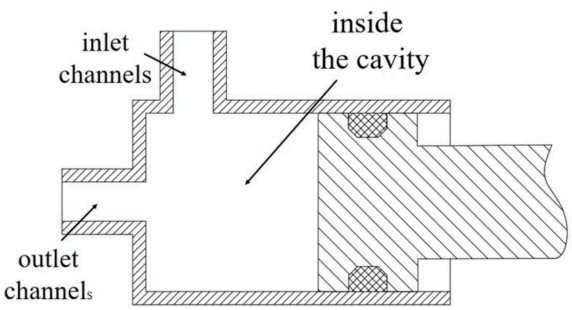


Figure 3. Simplified flow-domain model of the grease suction and discharge device.

The main parameters of the simplified flow channel are shown in Table 1:

Table 1. Key parameters of the suction and discharge device.

Component	Diameter (mm)	Length (mm)
inlet channels	3.4	5
outlet channels	3.4	5
inside the cavity	10	15

As shown in Figure 3, the simplified flow channel is a relatively common model for pipe flow. Research on pipe flow primarily focuses on issues such as the flow rate the pipe can handle, flow losses, and the required power.

2.2. Model Assumptions and Flow Equation for Grease in the Inlet Channel

The actual suction process is transient because the backward motion of the plunger continuously changes the working-chamber volume and pressure, causing the inlet velocity and volumetric flow rate to vary with time. However, to obtain an analytical relationship between the pressure gradient, grease rheological parameters, and inlet flow rate, the flow in the inlet channel is idealized as steady and fully developed.

The analytical model assumes that the grease is incompressible and isothermal and that the flow is laminar and axisymmetric. The inlet channel is simplified as a straight circular pipe with a constant cross-section. A continuous grease supply, a rigid no-slip wall, and single-phase flow are assumed, while air entrainment, gas dissolution, and leakage are neglected. Under the steady and fully developed assumptions, the axial velocity depends only on the radial coordinate, $u = u(r)$, where u is the axial velocity in $\mathrm{m \cdot s^{-1}}$ and r is the radial coordinate in m, and therefore

$$\frac{\partial u}{\partial t} = 0, \quad \frac{\partial u}{\partial z} = 0 \tag{1}$$

where t is time in s and z is the axial coordinate in m. The axial pressure gradient is balanced by the radial shear-stress distribution, allowing the velocity profile and volumetric flow rate to be derived using the steady Herschel–Bulkley constitutive equation.

It should be emphasized that this analytical model does not fully represent the actual suction stroke. During the real process, the grease accelerates as the plunger moves backward, and the transient term generally satisfies

$$\frac{\partial u}{\partial t} \neq 0 \tag{2}$$

In addition, the short inlet channel, inlet chamfer, and sudden connection to the working chamber may produce entrance effects, local contraction and expansion losses, axial velocity development, and three-dimensional flow redistribution. Therefore, the analytical solution is used only as an idealized theoretical reference for clarifying the effects of the pressure gradient and rheological parameters, whereas the transient CFD model is used to describe the actual suction process in greater detail.

Lubricating grease exhibits yield-stress and shear-thinning behavior. Accordingly, the Herschel–Bulkley model is adopted to describe its apparent rheological behavior [29]:

$$\tau = \tau_y + K\dot{\gamma}^n (\tau > \tau_y), \tag{3}$$

where τ represents shear stress in Pa, $\dot{\gamma}$ represents shear rate (velocity gradient) in s^{-1}, τ_y represents yield stress in Pa, K represents the consistency coefficient in Pa·s^n, and n represents the rheological index. The values of τ_y, K and n are listed in Section 3.3.

By performing a stress analysis on the grease in the inlet pipe of the suction and discharge device under a specific pressure difference, as shown in Figure 3, the results are presented in Figure 4:

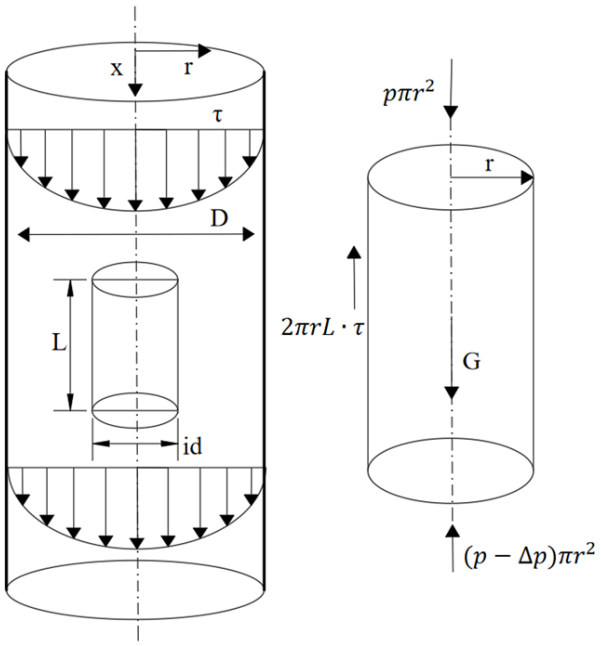


Figure 4. Stress analysis of grease at the inlet pipe.

Based on the force conditions governing the flow of general non-Newtonian fluids, consider a circular pipe of length L and radius R, in which the fluid flows in a fully developed, steady-state laminar flow. Consider a cylindrical fluid element coaxial with the pipe, with radius r ($0 \leq r \leq R$) and length L. This element is subjected to the following two forces in the direction of flow (assumed to be vertically downward) [30]:

$$\Delta p \cdot \pi r^2 - 2\pi rL \cdot \tau_w = 0, \tag{4}$$

Rearranging the formula yields

$$\tau_w = \frac{\Delta p}{2L} \cdot r, \tag{5}$$

where Δp denotes the pressure difference between the inlet and outlet ends of the pipe, with units of Pa., respectively, r is the radial coordinate in m, L is the channel length in m, and τ_w is the local shear stress in Pa.

Introducing the concept of equivalent pressure gradient, defined as

$$\nabla P_{eff} = \frac{L}{\Delta p}, \tag{6}$$

Substituting the equivalent pressure gradient into Equation (5), Equation (5) can be written as

$$\tau_w = \frac{\Delta p}{2L} \cdot r = \frac{r}{2} \cdot \left| \nabla P_{eff} \right|, \tag{7}$$

∇P_{eff} represents the pressure difference per unit length. Since pressure decreases in the direction of flow, $\Delta p = p_1 - p_2 > 0$; therefore, the effective pressure gradient ∇P_{eff} is

positive. In engineering applications, the absolute value is often used to ensure that the shear stress remains positive.

As shown in Figure 4, the suction line (vertical pipe) of the suction and discharge device is affected not only by the pressure difference between the two sections but also by gravity. Because the inlet channel is vertically oriented, Equation (7) is extended in the present study by including the signed gravitational body-force component. Therefore, the equivalent pressure gradient is revised as follows:

$$\nabla P_{eff} = \frac{dP}{dz} = \frac{\Delta p + \rho g L}{L}, \tag{8}$$

where ∇P_{eff} is the effective driving gradient in $\mathrm{Pa} \cdot \mathrm{m}^{-1}$, Δp is the pressure difference across the inlet channel in Pa, L is the inlet-channel length in m, ρ is the grease density in $\mathrm{kg} \cdot \mathrm{m}^{-3}$, and g is the signed gravitational acceleration component in $\mathrm{m} \cdot \mathrm{s}^{-2}$. From Equations (7) and (8), it can be seen that the shear stress is zero at the center of the pipe ($r = 0$), increases linearly with increasing radial distance r, and reaches its maximum value at the pipe wall ($r = R$). Due to the presence of the yield stress τ_y, when the radial position r is small, the shear stress τ_w at that location may be insufficient to overcome the fluid's internal resistance (i.e., $\tau_w < \tau_y$). Consequently, the fluid cannot undergo relative deformation and instead moves as a plug flow. As r increases, the shear stress gradually rises; once it exceeds the yield stress, the fluid begins to undergo shear flow [31]. Therefore, within the pipe cross-section, the fluid is divided into two regions with different properties: the central plug flow region and the shear flow region, as shown in Figure 5. The central plug flow region is located near the center of the pipe, with a range of $0 \leq r \leq r_c$. Within this region, $\tau(r) \leq \tau_y$, the internal shear rate $\dot{\gamma} = 0$, and the fluid translates as a whole at a constant velocity, similar to the motion of a rigid body. The shear flow zone is located outside the plug flow zone, with a range of $r_c \leq r \leq R$. Within this zone, $\tau(r) \geq \tau_y$, the fluid undergoes shear deformation, and the velocity exhibits a radial gradient distribution.

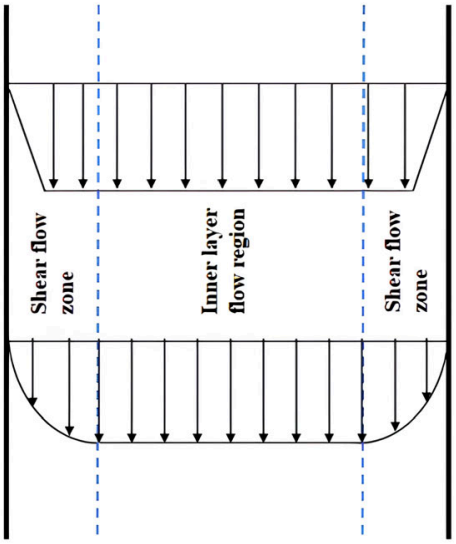


Figure 5. Flow in the inlet channels.

The critical radius, r_c marks the boundary between the plug-flow region and shear-flow region. Based on the condition that the shear stress distribution equals the yield stress, by deriving Equations (7) and (8), we obtain the formula for the critical radius is

$$r_c = \frac{2\tau_y}{\nabla P_{eff}}, \tag{9}$$

where r_c is the radius of the unyielded plug region in m. When $\tau_y \neq 0$, the pipe cross-section can be divided into a central plug-flow region and an outer shear-flow region. In the plug-flow region, the local shear stress is lower than the yield stress, and the grease moves as an unyielded plug with an approximately uniform velocity. In the shear-flow region, the local shear stress exceeds the yield stress, and the velocity decreases gradually from the plug-flow boundary toward the pipe wall. Therefore, the yield stress determines the size of the plug-flow region and directly affects the suction flow rate of grease in the inlet channel.

2.3. Velocity Distribution and Volumetric Flow Rate in the Inlet Channel

Based on the stress distribution and the H–B constitutive model, the velocity profiles in the plug-flow and shear-flow regions are derived separately in the present study. The total volumetric flow rate is then obtained by integrating the resulting piecewise velocity profile over the channel cross-section:

$$Q = \int_0^R udA = \int_0^R 2\pi \cdot urdr, \tag{10}$$

where Q is the volumetric flow rate, expressed in $m^3 \cdot s^{-1}$; $u(r)$ is the local axial velocity, expressed in $m \cdot s^{-1}$; A is the cross-sectional area of the inlet channel, expressed in m^2; and r and R are the radial coordinate and inlet-channel radius, respectively, both expressed in m.

For a yield-stress fluid, the cross-section contains both a plug-flow region and a shear-flow region. Therefore, the total volumetric flow rate cannot be obtained by multiplying the average velocity by the area directly; instead, it should be calculated by integrating the radial velocity distribution.

In the plug-flow region ($0 \leq r \leq r_c$), the grease is unyielded and moves with a uniform axial velocity. This velocity is equal to the velocity at the boundary between the plug-flow and shear-flow regions. Therefore, the plug-flow velocity is given by

$$u_{max} = u(r_c) = \frac{n}{n+1}\left(\frac{\nabla P_{eff}}{2K}\right)^{1/n}(R - r_c)^{\frac{n+1}{n}}, \tag{11}$$

In the equation, u_{max} is the flow velocity in the central plug flow region in $m \cdot s^{-1}$, n is the rheological index, ∇P_{eff} is the equivalent pressure gradient, K is the consistency coefficient, R is the pipe radius, and r_c is the critical radius expressed in m.

In the shear-flow region ($r_c < r \leq R$), the shear stress is higher than the yield stress, and the grease behaves as a yielded material. The velocity reaches its maximum value at the plug-flow boundary and decreases toward the wall. Considering the no-slip boundary condition at $r = R$, the velocity distribution in this region is given by

$$u(r) = \frac{n}{n+1}\left(\frac{\nabla P_{eff}}{2K}\right)^{1/n}\left[(R - r_c)^{\frac{n+1}{n}} - (r - r_c)^{\frac{n+1}{n}}\right], \tag{12}$$

In this equation, $u(r)$ represents the flow velocity at point r in the shear flow zone in $m \cdot s^{-1}$, n is the rheological index, ∇P_{eff} is the equivalent pressure gradient, K is the consistency coefficient, R is the pipe radius, and r_c is the critical radius.

The total volumetric flow rate Q of the grease inlet pipe of the suction and discharge device can be calculated by integrating the cross-sectional velocity profile over the area:

$$Q = \int_0^R 2\pi r \cdot u(r)dr = \pi r_c^2 u_{max} + 2\pi \int_{r_c}^R r \cdot u(r)dr \tag{13}$$

where Q is the volumetric flow rate in $m^3 \cdot s^{-1}$. For comparison with the simulation results, it was converted to $mL \cdot s^{-1}$ using $1\ m^3 \cdot s^{-1} = 10^6\ mL \cdot s^{-1}$. Therefore, Equation (13) provides an idealized steady-flow reference for the subsequent CFD analysis.

3. Analysis of the Rheological Properties of Grease

3.1. Grease Material and Rheological Modeling Basis

Lubricating grease is a typical semi-solid lubricant composed of base grease, thickener, and additives [32]. The thickener forms a three-dimensional network structure that retains the base grease and gives grease its yield-stress and shear-dependent flow behavior. For lithium-complex grease, the thickener network is relatively stable and provides good mechanical stability and high-temperature resistance [33,34]. However, during suction through a narrow inlet channel, this network structure also causes nonlinear flow resistance, especially under low-temperature or low-shear conditions.

The main non-Newtonian characteristics relevant to the suction process are yield stress and shear thinning. The yield stress determines whether the grease can be initiated under a given pressure difference, while shear thinning reduces the apparent viscosity as the shear rate increases. Although grease may also exhibit thixotropy, the present study focuses on the apparent steady-state relationship between shear stress and shear rate. Therefore, the time-dependent structural breakdown and recovery of grease are not included in the current model.

Considering the applicability of the active waste-grease recovery system in wind turbine bearing lubrication, Mobil SHC Grease 460 WT was selected as the test grease in this study. Mobil SHC Grease 460 WT is a high-performance synthetic lithium-complex grease designed for wind turbine applications. It is suitable for the lubrication of main bearings, pitch bearings, and yaw bearings, and can be applied either by manual greasing or through centralized grease systems and grease dispensers. The grease has good high- and low-temperature performance, excellent pumpability, structural stability in the presence of water, and protection against wear, rust, and corrosion. Therefore, it was selected as a representative wind-turbine bearing grease for evaluating the suction performance of the grease suction–discharge device. The typical performance parameters of Mobil SHC Grease 460 WT are shown in Table 2.

Table 2. Typical performance parameters of grease.

Item	Performance Parameter
Operating temperature range/°C	−30–150
NLGI	1.5
Thickener type	Lithium complex
Worked penetration at 25 °C/0.1 mm	305
Dropping point/°C	255
Base grease viscosity at 40 °C/$mm^2 \cdot s^{-1}$	460
Density/$kg \cdot m^{-3}$	870

3.2. Rheological Test Method

The Anton Paar MCR302 Rotational Rheometer (Anton Paar (China) Co., Ltd., Shanghai, China) is an advanced laboratory instrument (as shown in Figure 6) primarily used to measure the rheological parameters of various materials, such as liquids and soft solids, in order to evaluate their rheological properties. The instrument offers a wide measurement range, with rotational speeds ranging from 10^{-6} to 200 rpm, torque ranging from 10 μN·m to 0.2 N·m, and normal force ranging from 0.001 to 50 N. It is equipped with the Rheo Compass application, an advanced rheological testing and analysis software developed by

Anton Paar. This software breaks down complex rheological testing processes into multiple projects and modules, covering functions, such as test procedures, graphs, data, display, analysis, and report templates, and is capable of handling complex rheological models and predicting rheological properties.



Figure 6. MCR302 Rotational Rheometer.

Temperature and viscosity are among the key environmental factors affecting the rheological properties of grease. The viscosity of the same grease varies at different temperatures. To accurately determine the shear stress and viscosity behavior of the grease at a specific temperature [35], it is necessary to conduct flow characteristic tests on the grease. Flow characteristic tests involve controlling variations in shear rate to analyze how the shear stress and viscosity of the grease change under sustained shear stress as a function of shear rate, and to plot the corresponding shear stress-shear rate and viscosity shear rate flow curves. To ensure the reliability of the calculation results, this study selected temperature conditions commonly encountered during machine operation to conduct the tests on this grease, specifically setting the temperatures to 5 °C, 25 °C, and 45 °C.

In the flow characteristics test, shear rates were controlled between 0.1 and 100 s^{-1}. A parallel-plate rotor system with a plate diameter of 25 mm and a gap of 1 mm was used. After loading the sample, excess grease around the plate edge was carefully removed to ensure proper filling of the measuring gap. During each shear-rate sweep, the sample edge was visually monitored, and no visible sample recession or partial emptying of the measuring gap was observed over the investigated shear-rate range [36]. Three temperature conditions, 5 °C, 25 °C, and 45 °C, were selected to simulate shear variations under actual operating conditions. By measuring the shear stress and viscosity of the grease under sustained shear, shear stress-shear rate curves and viscosity-shear rate curves were plotted to obtain key rheological parameters such as viscosity, shear stress, and shear rate.

3.3. Flow-Curve Results and H-B Model Fitting

The flow characteristics of grease directly affect the operational performance of grease extractors. In particular, at different temperatures, grease exhibits varying degrees of softening, hardening, and grease separation, which in turn leads to variations in the grease extraction performance of the extractor. These performance variations not only increase the operational load on the system but also affect the operational stability and reliability of the grease extractor. By conducting in-depth research on the flow behavior of grease under external forces and understanding its stress-response characteristics under varying temperatures and shear conditions, it is possible to accurately and comprehensively study the flow state of grease within the suction and discharge unit. The variations in shear stress and viscosity of the grease as a function of shear rate at different temperatures are shown in Figures 7 and 8.

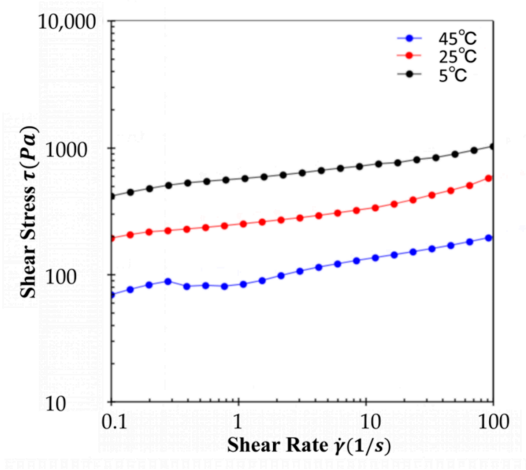


Figure 7. Variation in shear stress with shear rate.

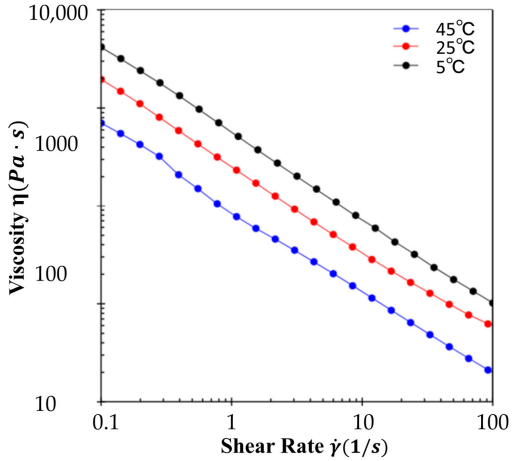


Figure 8. Variation in viscosity with shear rate.

Figures 7 and 8 show that, across different temperature ranges, the shear stress of this grease increases with increasing shear rate; furthermore, at a constant shear rate, a decrease in temperature leads to a significant increase in shear stress, indicating that low temperatures increase the fluids flow resistance. The viscosity curves show that the apparent viscosity of all samples decreases sharply with increasing shear rate, exhibiting a clear decreasing trend in a double-logarithmic coordinate system, demonstrating typical shear-thinning behavior. At the same time, an increase in temperature shifts the viscosity curve downward overall. This is because heating enhances molecular thermal motion and weakens intermolecular interactions, thereby significantly reducing the viscosity of the

system. Overall, the flow behavior of this grease conforms to the power-law model and exhibits strong temperature sensitivity.

The measured shear-stress data were fitted using the Herschel–Bulkley model defined in Equation (3). Nonlinear regression was used to determine the yield stress τ_y, consistency coefficient K, and flow-behavior index n at each temperature. The fitting results are listed in Table 3.

Table 3. H-B fitting of grease at different temperatures.

Temperature	Fitting the Equation
5 °C	$\tau = 410.43 + 113.5\dot{\gamma}^{0.37}$
25 °C	$\tau = 216.65 + 26.5\dot{\gamma}^{0.59}$
45 °C	$\tau = 50.60 + 8.5\dot{\gamma}^{0.54}$

The steps for fitting the H-B model are as follows:

1. Import the shear stress and viscosity data at different temperatures into Origin software and write a fitting program.
2. Run the fitting program to fit the experimental data to the H-B model and obtain the optimal parameters τ_y, K, and n.
3. Perform a predictive analysis of the fitting results to predict the shear stress and viscosity of the grease at different shear rates, and verify the accuracy of the fitting equation by comparing the predictions with the experimental data.

The rheological fitting results for grease at different temperatures are shown in Table.

3.4. Analytical Calculation Based on Fitted H-B Parameters

The Herschel–Bulkley parameters measured at 25 °C were substituted into the analytical inlet-channel model developed in Section 2.3. The temperature of 25 °C was selected as the reference condition for comparison with the baseline CFD simulation. Using MATLAB, version R2024b, the theoretical volumetric flow rate was calculated over the investigated range of pressure differences. The analytical results, which represent the idealized inlet-channel condition defined in Section 2, are shown in Figure 9.

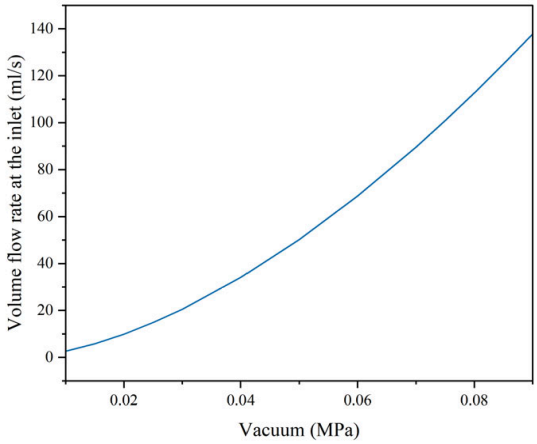


Figure 9. MATLAB calculation results.

As shown in Figure 9, the volumetric flow rate increases as the vacuum level rises. When the model of the suction and discharge unit, the type of grease, and the pipe radius are all held constant, the flow rate is directly proportional to the flow velocity; that is, the higher the flow rate, the faster the flow velocity, and the faster the grease inflow, which means the filling process can be completed more quickly.

4. Development of a Numerical Simulation Model for a Plunger Pump Using FLUENT

4.1. 3D Modeling and Mesh Generation for Plunger Pumps

Based on the simplified flow domain defined in Section 2.1, a three-dimensional computational model was established in SolidWorks version 2024. The model included the inlet channel, working chamber, discharge channel, and the deforming fluid region associated with plunger motion. The resulting computational domain is shown in Figure 10.

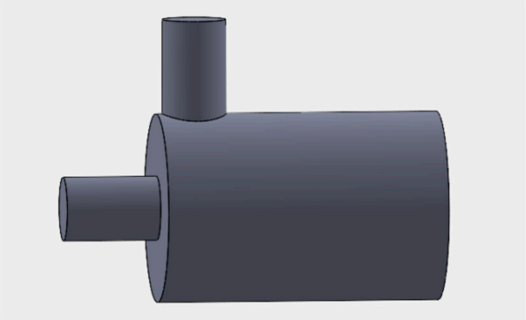


Figure 10. 3D computational domain used for CFD simulations.

The fluid domain was discretized using a hybrid tetrahedral–hexahedral mesh. Local mesh refinement was applied to the grease inlet, the chamfered transition, the junction between the inlet channel and the working chamber, where relatively large pressure, velocity, and apparent-viscosity gradients were expected. Seven inflation layers were generated along the no-slip walls. The first-layer thickness was 0.008 mm and the growth rate was 1.10. The initial computational mesh contained 170,608 cells and 81,602 nodes. The overall mesh and the locally refined mesh are shown in Figure 11.

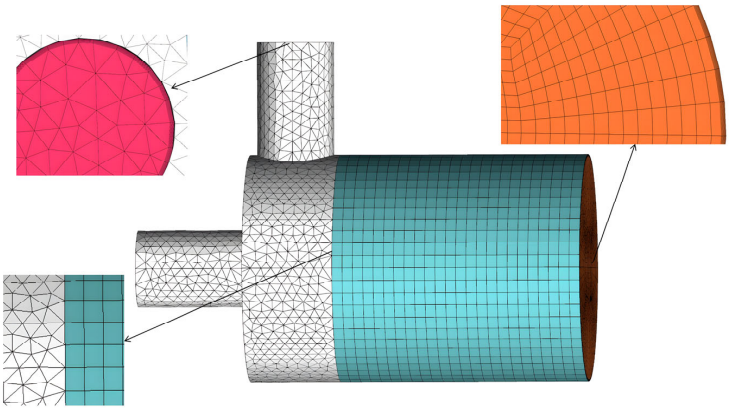


Figure 11. Fluid domain meshing.

The mesh exhibited satisfactory overall quality, with most cells falling within the high-quality range. The minimum orthogonal quality was 0.47. Following the numerical methodology commonly adopted in CFD studies of hydraulic pipelines [37], a mesh-independence study was conducted to evaluate the sensitivity of the predicted inlet flow rate to spatial discretization. Three mesh systems with progressively increasing element counts—Coarse (93,527 cells), Medium (170,608 cells), and Fine (415,739 cells)—were generated and tested. The inlet volumetric flow rate was selected as the evaluation criterion. As shown in Table 4, the variation between the Medium and Fine meshes was only 0.19%. This confirms that the Medium mesh provides sufficient resolution for accurate predictions. Considering the balance between computational accuracy and time cost, the Medium mesh (170,608 cells) was adopted for all subsequent simulations.

Table 4. Results of the mesh independence study.

Mesh Type	Number of Cells ($\times 10^4$)	Inlet Flow Rate ($mL \cdot s^{-1}$)	Change from Previous (%)	Remarks
Coarse	9.35	67.152	−2.98%	compared to the center grid
Medium	17.06	69.215	0%	this paper selects
Fine	41.57	69.447	0.33%	compared to the center grid

4.2. Setting Boundary Conditions in FLUENT

The transient grease flow in the suction and discharge device was simulated using the pressure-based solver in ANSYS Fluent (version 2024R1). The grease was treated as an incompressible and isothermal non-Newtonian fluid, and the laminar-flow model was adopted. A single-phase model was adopted, assuming a continuous grease supply at the inlet. Air entrainment, gas dissolution, and leakage through the device connections were not considered in the computational domain. Its density was set to 870 kg/m^3, while the apparent viscosity was determined using the temperature-dependent Herschel–Bulkley parameters obtained from the rheological tests at 5, 25, and 45 °C. The operating pressure was set to 101,325 Pa. Gravity was included in the numerical model, with an acceleration of 9.81 m/s^2 directed vertically downward along the inlet channel.

The inlet was defined as pressure boundaries, and their pressure values were specified according to the investigated vacuum conditions. All other solid surfaces were treated as smooth no-slip walls. The reciprocating motion was represented using the dynamic-mesh method. The surface was defined as a moving rigid wall, while the adjacent fluid region was treated as a deforming zone. Mesh smoothing and local remeshing were employed to maintain acceptable mesh quality during movement.

Pressure and velocity were coupled using the Coupled algorithm. Spatial gradients were evaluated using the least-squares cell-based method. The pressure and momentum equations were discretized using the second-order and second-order upwind schemes, respectively, while a second-order implicit scheme was adopted for temporal discretization. The convergence criterion for the continuity and velocity residuals was set to 10^{-4}, and the inlet volumetric flow rate was monitored to ensure that the transient solution was stable.

4.3. Comparison of Theoretical Calculations and Simulation Results

To examine the consistency between the CFD simulation and the idealized analytical prediction, the grease flow in the inlet channel at 25 °C was analyzed under different vacuum levels. Using the fitted Herschel–Bulkley parameters, the volumetric flow rate at the inlet was calculated by the analytical model and compared with the corresponding FLUENT simulation results, as shown in Figure 12.

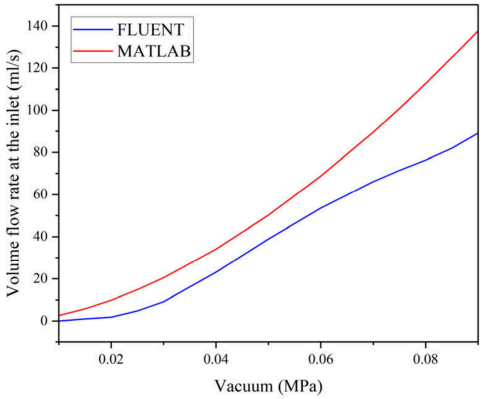


Figure 12. Comparison of FLUENT and MATLAB analysis results.

As shown in Figure 12, both the analytical calculation and the FLUENT simulation show an increasing trend in inlet volumetric flow rate with increasing vacuum level. This indicates that the CFD simulation captures the same general influence of vacuum level on grease suction as predicted by the analytical model. However, the analytical model is based on an ideal straight circular inlet channel and assumes that the applied pressure difference acts completely across the inlet channel, whereas the FLUENT model considers the actual flow-domain geometry, entrance effects, local expansion, and chamber flow. Therefore, the difference between the two results is reasonable.

The analytical calculation generally gives a higher flow rate than the FLUENT simulation, which can be attributed to the neglect of local pressure losses and three-dimensional flow effects in the analytical model. Thus, this comparison should be regarded as a numerical consistency check rather than a strict validation of the CFD model. The FLUENT model is subsequently used to analyze the detailed flow-field characteristics and parameter effects of the grease suction–discharge device.

4.4. Analysis of Internal Flow Field Characteristics

For typical operating conditions, numerical simulations of the flow characteristics of grease within the suction and discharge device were conducted using FLUENT software. During the simulation, the ambient temperature was set to 25 °C and the system vacuum to 0.07 MPa, establishing these as the typical operating conditions.

4.4.1. Pressure Distribution

Figure 13 shows the pressure distribution contour plot during the grease suction process of the suction and discharge device while it is in operation. As can be seen from Figure 13, the pressure is relatively high in the inlet region of the device. This is because, during grease suction process, the fluid at the inlet is rapidly drawn in, resulting in higher pressure in this area and providing the necessary pressure gradient for the suction of the grease. At the initial stage shown in Figure 13a, the pressure difference is mainly concentrated near the inlet channel, and the pressure field in the working chamber has not yet fully developed. As the suction process continues, as shown in Figure 13b,c, the pressure influence gradually extends from the inlet channel to the working chamber, and local pressure variations appear near the connection between the inlet channel and the chamber. At the later stage shown in Figure 13d, the pressure field becomes relatively more stable as more grease enters the chamber, but the pressure distribution is still not completely uniform near the inlet–chamber junction. At the bends and narrow sections of the flow channel, the pressure distribution exhibits localized fluctuations and changes. This is primarily due to changes in fluid velocity as the fluid flows through these complex geometric structures, resulting in the conversion of kinetic energy into pressure energy and vice versa.

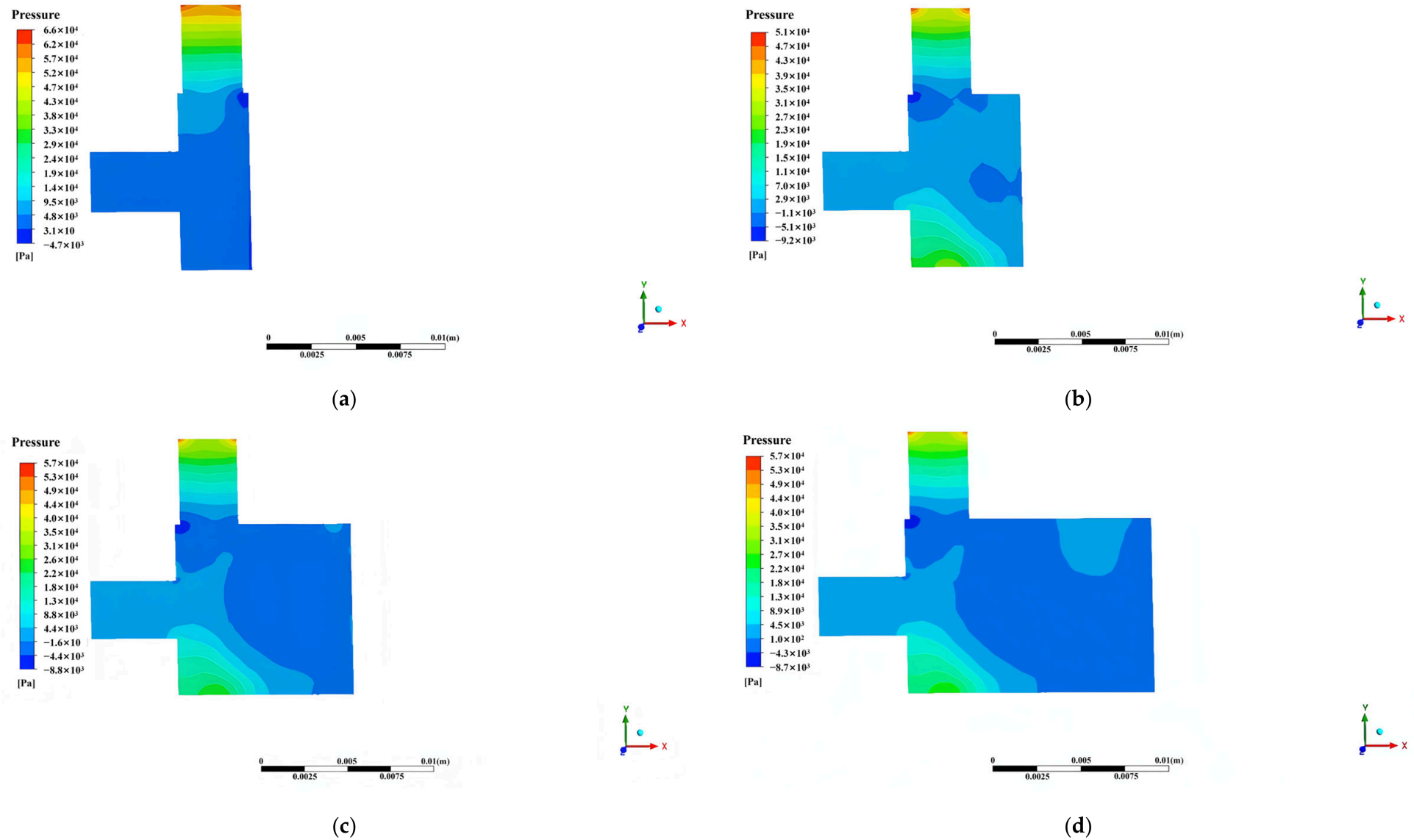


Figure 13. Pressure distribution at different times under typical operating conditions. (**a**) 0.001 s; (**b**) 0.012 s; (**c**) 0.024 s; and (**d**) 0.036 s.

4.4.2. Flow Velocity Distribution

Figure 14 shows the velocity distribution contour plot of the grease suction process during operation of the suction and discharge device. As can be seen from Figure 14, the velocity distribution of the grease within the suction and discharge device follows a certain pattern: the velocity near the suction port is relatively high, as this area is directly subjected to vacuum pressure, causing the grease to be rapidly drawn in. At the initial stage shown in Figure 14a, the velocity is mainly concentrated in the inlet channel, and only a small amount of grease enters the working chamber. As the suction process continues, as shown in Figure 14b,c, the high-velocity region gradually extends from the inlet channel into the chamber, and the grease begins to spread inside the chamber. However, at the point where the suction port contacts the chamber, the grease distribution is relatively sparse, which hinders its smooth entry. In the later stage shown in Figure 14d, the grease further spreads inside the chamber, but the velocity distribution remains non-uniform. Furthermore, once the grease enters the chamber, it forms distinct vortices, and this flow pattern also hinders the smooth entry of the grease.

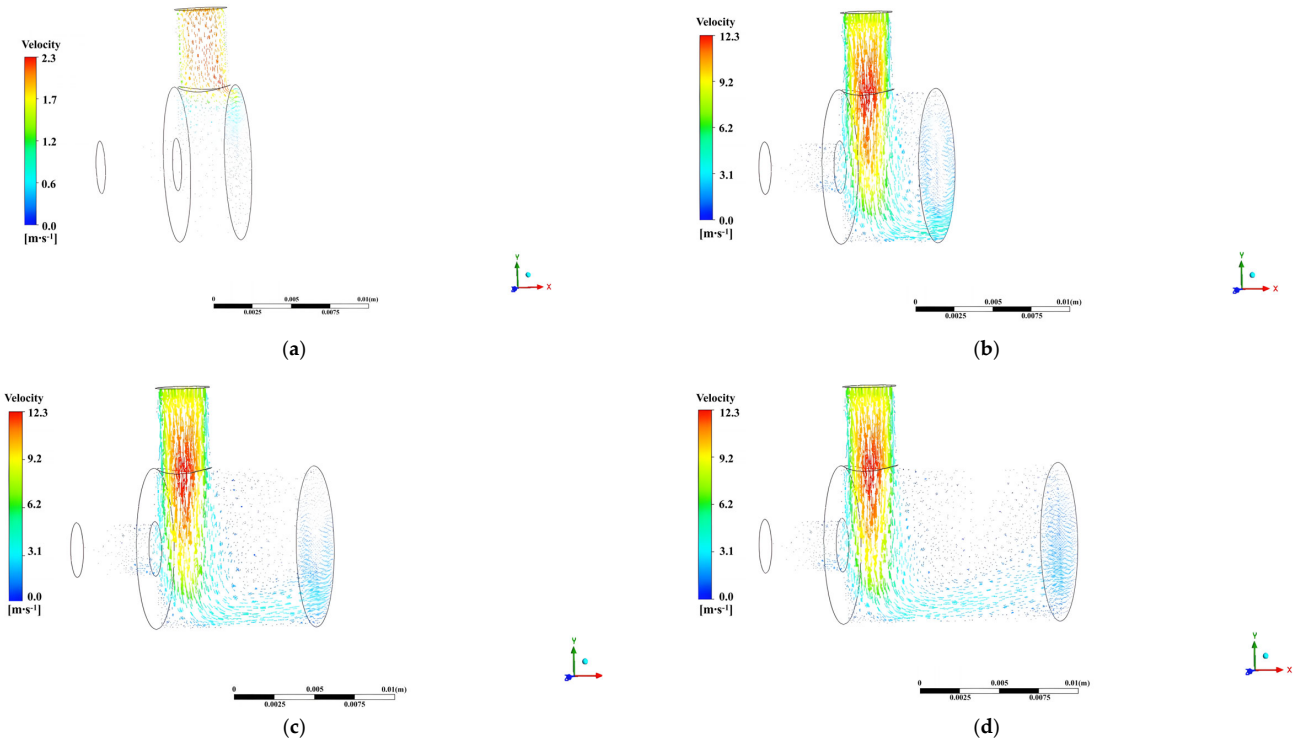


Figure 14. Velocity distribution at different times under typical operating conditions. (**a**) 0.001 s; (**b**) 0.012 s; (**c**) 0.024 s; and (**d**) 0.036 s.

5. Multifactorial Analysis of Plunger Pump Performance Based on Orthogonal Experiments

5.1. Orthogonal Experimental Design

5.1.1. Determination of Experimental Factors and Selection of Level Categories

To address the issues of grease spillage and replacement during the grease change process for wind turbine bearings, and taking into account the movement of grease within the bearings, vacuum-assisted grease replacement technology is employed. This method alters the vacuum level inside the bearing to create negative pressure, thereby expelling the degraded grease from the bearing cavity [38]. Based on the suction mechanism described in Section 2.1, the rheological results presented in Section 3, and the baseline flow-field analysis in Section 4.4, three controllable factors were selected for the orthogonal design:

vacuum level (Factor A), grease temperature (Factor B), and inlet chamfer radius (Factor C). Vacuum level determines the driving pressure difference, grease temperature affects the rheological parameters and flow resistance, and chamfer radius influences the local flow behavior at the inlet. Other factors, including vibration, grease contamination, and operating impact, were not included because they are difficult to quantify or control within the scope of the present numerical study. A blank column, Factor D, was reserved for error estimation. The selected factors and levels are described below.

Vacuum Level During Operation of the Suction and Discharge Device for Grease (A): Accumulation of old grease inside the bearing creates pressure, preventing new grease from being injected; vacuum-assisted suction and discharge of grease eliminates this pressure, ensuring the internal cavity remains unobstructed. The negative pressure generated by vacuum extraction effectively draws waste grease from the bearing's interior through the grease drain hole, preventing it from accumulating, hardening, or coking inside the bearing. This ensures that fresh grease can be injected smoothly and perform its lubricating function. Based on this, to better investigate the impact of vacuum level on the performance of the suction and discharge device, this study simplifies the vacuum environment of the device by replacing variations in the vacuum environment with negative pressure settings, and determines the negative pressure values for vacuum extraction to be 0.01–0.09 MPa. Considering actual operational requirements and bearing grease seal pressure, vacuum levels of 0.05 MPa, 0.07 MPa, and 0.09 MPa were selected.

Grease Viscosity (B): Wind-turbine bearings operate under varying ambient and internal temperature conditions, which can substantially affect the rheological behavior and transport resistance of lubricating grease. At lower temperatures, the yield stress and apparent viscosity of the grease generally increase, making it more difficult for the grease to enter the suction chamber. As temperature rises, grease viscosity decreases; however, the relationship between grease viscosity and temperature is not linear but follows a specific curvilinear trend. It is necessary to select an appropriate grease based on its specific properties and operating environment to ensure it maintains suitable viscosity and lubrication performance within the operating temperature range. Within the available experimental conditions, given that wind turbines generally operate within a wide temperature range, ranging from −30 °C to 85 °C, this paper selects three representative temperatures—low-temperature startup (5 °C), ambient temperature (25 °C), and rated operating temperature (45 °C)—to comprehensively examine the rheological properties of the grease under various typical operating conditions. The study investigates the corresponding changes in viscosity and analyzes the flow behavior of the grease under these three conditions. It should be noted that sub-zero rheological measurements were not included in the present study; therefore, the discussion of low-temperature suction performance is limited to the tested temperature range.

Chamfer Radius (C) of the Grease Inlet Pipe: Grease is a non-Newtonian fluid characterized by yield stress and shear thinning; it is more sensitive to local geometric changes in flow channels than Newtonian fluids. The abrupt geometric transition at the inlet of the grease pipe, combined with the absence of a chamfer, causes significant local resistance losses as the grease flows through this section. This makes it prone to flow separation and the formation of vortex regions, thereby reducing the effective intake area. Analysis of pressure and velocity contour plots reveals that, in the absence of a chamfer at the inlet, a sudden drop in pressure at the inlet edge creates a local low-pressure zone. This results in disordered velocity vectors, causing a portion of the fluid to flow backward and generate vortices. These vortices dissipate energy, leading to an unstable flow state as the grease enters the pump chamber and thereby affecting the efficiency of the grease suction and discharge unit. Therefore, the chamfer radius of the grease inlet pipe is a

critical geometric parameter affecting the internal flow field characteristics of the suction and discharge device; its magnitude is related to local pressure loss, the extent of the vortex zone, and the effective suction area. To investigate the impact of different chamfer radii on the performance of the suction and discharge device, this experiment will analyze chamfer radii of 0 mm, 0.85 mm, and 1.7 mm.

As a non-Newtonian fluid characterized by yield stress and shear thinning, grease is far more sensitive to local geometric changes in flow channels than Newtonian fluids. Geometric abrupt changes at the inlet of the grease supply pipe, such as the absence of a chamfer, cause significant local resistance losses as the grease flows through this area. This also facilitates the formation of flow separation and vortex zones, thereby reducing the effective suction area. Analysis of pressure and velocity contour plots reveals that when the inlet of the grease supply pipe lacks a chamfer, a sharp drop in pressure occurs at the inlet edge, creating a local low-pressure zone. Meanwhile, the velocity vectors in this region become disordered, and some fluid even exhibits backflow, leading to the formation of vortices. These vortices not only consume energy but also destabilize the flow of grease as it enters the pump chamber, affecting subsequent grease suction and discharge efficiency. Therefore, the chamfer radius of the grease inlet pipe is one of the key geometric parameters influencing the internal flow field characteristics of the suction and discharge device; its magnitude directly affects the magnitude of local pressure loss, the extent of the vortex zone, and the size of the effective suction area. To investigate the impact of different chamfer radii on the performance of the suction and discharge device, this experiment will examine various chamfer radius levels.

5.1.2. Experimental Scheme

An orthogonal experiment is a design method used to study multiple factors and multiple levels. It employs an orthogonal table to comprehensively plan experimental designs, conduct comprehensive comparisons, and perform statistical analyses. By rationally arranging the factors and levels in the experiment, orthogonal experimental designs can effectively identify and evaluate the primary effects of each factor on the experimental results, as well as the interactions among factors. In contrast, a full factorial experiment involves testing all possible combinations of all factors and levels [39]. Therefore, when the number of factors and levels is large, the number of trials required for a full factorial experiment increases dramatically. This not only results in high experimental costs but also consumes a significant amount of time, making it difficult to implement in practice. Based on the results of orthogonal experiments, optimal combinations of factor levels can be quickly identified, thereby providing effective optimization strategies and guidance for fields such as actual production and scientific research.

In this study, an orthogonal experimental design was employed. Common orthogonal experimental designs include L4 (2^3), L9 (3^4), L12 (2^{11}), and L16 (4^5). In this example, in addition to examining the effects of factors A, B, and C, the influence of the blank column *D* (error) must also be considered. Each factor has three levels; there are three factors in total, and each factor has 2 degrees of freedom. Since the experiment must account for the effect of the blank column, the blank group has 2 degrees of freedom; therefore, the total degrees of freedom are 8. According to the principle that the degrees of freedom of an orthogonal design must be no less than the sum of the degrees of freedom of each factor and the blank column, and in accordance with the criterion of selecting the smallest orthogonal design, the L9 (3^4) orthogonal design was ultimately chosen for this experiment [40]. The experimental data are shown in Table 5.

Table 5. Orthogonal Experiment Table.

Number	A	B	C	Blank Column
1	0.05	5	0	1
2	0.05	25	0.85	2
3	0.05	45	1.7	3
4	0.07	5	0.85	3
5	0.07	25	1.7	1
6	0.07	45	0	2
7	0.09	5	1.7	2
8	0.09	25	0	3
9	0.09	45	0.85	1

5.2. Analysis of Orthogonal Experiment Simulation Results

There are typically two methods for analyzing the results of orthogonal experiments. The first is the visual analysis method, also known as range analysis. The second is analysis of variance (ANOVA). This study employs both methods to analyze the experimental results and verify the optimal results.

5.2.1. Range Analysis

In this study, the vacuum pressure (A) of the suction and discharge device during operation was set at 0.05 MPa, 0.07 MPa, and 0.09 MPa; the grease viscosity (B) was set at 5 °C, 25 °C, and 45 °C; the chamfer radius (C) of the grease inlet pipe was set at 0 mm, 0.85 mm, and 1.7 mm, with a blank column serving as a four-factor, three-level design. The volumetric flow rate curve at the inlet of the suction and discharge device exhibits an approximately parabolic shape. Its peak value serves as an approximate measure of the volume of grease drawn into the device within a specific time period. Therefore, the maximum value of the inlet volumetric flow rate during operation is used as the response variable for the orthogonal experiment. The steps for range analysis are as follows: First, sum the results of each test for each factor at level 1 and calculate the average of these sums, denoted as $k1$. Next, sum the corresponding results for level 2 and calculate the average, denoted as $k2$. Continue this process to obtain the average of all level sums. Then, determine the maximum value k_{max} and the minimum value k_{min}; the difference between the two is the range R. Finally, rank the factors from largest to smallest based on R to determine the degree of their influence. The results of the range analysis are shown in Table 6.

Table 6. Range Analysis Table for Orthogonal Experiments.

Number	A	B	C	Blank Column	Result (mL·s^{-1})
1	0.05	5	0	1	23.128
2	0.05	25	0.85	2	45.701
3	0.05	45	1.7	3	94.338
4	0.07	5	0.85	3	44.894
5	0.07	25	1.7	1	78.411
6	0.07	45	0	2	98.735
7	0.09	5	1.7	2	67.675
8	0.09	25	0	3	86.148
9	0.09	45	0.85	1	126.442
$k1$	54.389	45.232	69.337	75.994	
$k2$	74.013	70.087	72.346	70.704	
$k3$	93.422	106.505	80.141	75.127	

Table 6. *Cont.*

Number	A	B	C	Blank Column	Result (mL·s^{-1})
R	39.033	61.273	10.804	5.29	
Sort	2	1	3	4	

As shown in Table 6, the range values for grease temperature, vacuum level, and inlet chamfer radius were 61.273, 39.033, and 10.804 mL·s^{-1}, respectively. Therefore, within the investigated ranges, the influence of the three factors on the maximum inlet volumetric flow rate followed the order: grease temperature (B) > vacuum level (A) > inlet chamfer radius (C). The mean response increased from k1 to k3 for all three factors. Accordingly, the level combination predicted to maximize the inlet volumetric flow rate was A3B3C3, corresponding to a vacuum level of 0.09 MPa, a grease temperature of 45 °C, and an inlet chamfer radius of 1.7 mm.

5.2.2. Analysis of Variance

Analysis of variance is designed to distinguish between variations in experimental results caused by differences in the levels of the factors under study and those caused by experimental error. This allows for a deeper investigation into which factors influence the results and which do not, thereby identifying the major and minor factors. The results are shown in Table 7.

Table 7. Analysis of Variance for an Orthogonal Experiment.

Factors	Sum of Squared Deviations	Degrees of Freedom	Mean Square	*F*-Number	Threshold F	Significance
A	2285.347	2	1142.673	47.317	0.0207	**
B	5698.373	2	2849.186	117.982	0.0084	***
C	186.558	2	93.279	3.863	0.2056	*
D (error)	48.299	2	24.149			

According to the results of the analysis of variance (ANOVA) for the orthogonal experiment in Table 7, the significance levels are indicated as: $p < 0.05$ (**) and $p < 0.01$ (***). The sum of squares for temperature (Factor B) is the largest, with a corresponding significance probability of 0.0084, which is less than 0.01, indicating that the effect of temperature on the outlet flow rate of the suction and discharge device is highly significant (***); The sum of squares for vacuum was 2285.347, with a corresponding significance probability of 0.0207, which is less than 0.05, indicating a significant effect (**); the sum of squares for chamfer angle (Factor C) was the smallest, with a corresponding significance probability of 0.2056, which is greater than 0.05, suggesting that its effect on flow rate is not significant (*), with only a weak trend of influence. Additionally, the sum of squares for the error term is small (48.299), indicating that experimental random errors are well controlled and the results are reliable. Overall, the order of influence of each factor on the outlet flow rate is temperature > piston clearance > chamfer angle, with temperature being the decisive factor, followed by vacuum level, and the chamfer angle contributing minimally. Therefore, in practical engineering applications, to improve the delivery efficiency of the suction and discharge device, priority should be given to optimizing the operating temperature, followed by adjusting the piston clearance, while the chamfer angle can be selected according to standard machining practices.

5.3. Discussion of the Patterns of How Factors Affect Performance

Based on the range of data, a sensitivity analysis was conducted on each influencing factor. Figure 15 shows a statistical chart illustrating the sensitivity of the volumetric flow rate at the inlet to each influencing factor.

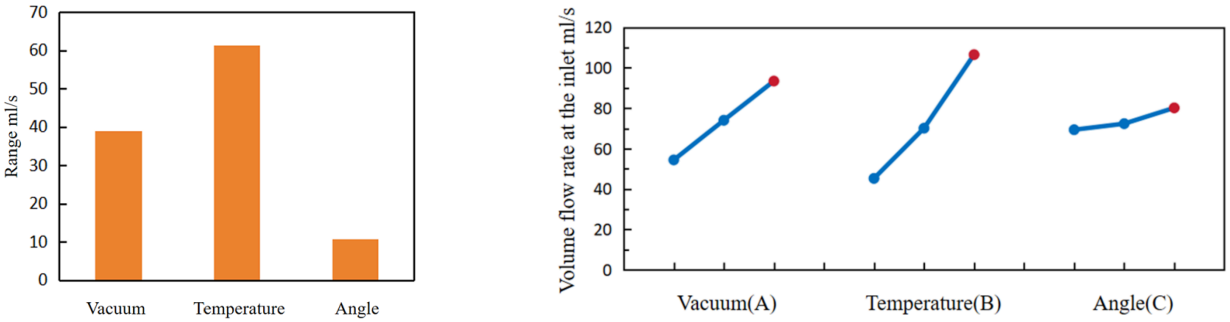


Figure 15. Effect of various factors on inlet flow rate. (**a**) effect of factors on volumetric flow rate at the inlet; (**b**) volume flow rate at the inlet for different levels of each factor.

Figure 15 illustrates the response of the maximum inlet volumetric flow rate to the three investigated factors. The strong temperature dependence can be attributed to the substantial changes in the rheological properties of the grease. As temperature increases, the yield stress and apparent viscosity decrease, reducing the resistance to flow through the inlet channel.

Increasing the vacuum level increases the driving pressure difference across the inlet channel. The resulting increase in the pressure gradient promotes grease yielding and increases the inlet velocity and volumetric flow rate.

The inlet chamfer radius mainly affects the local flow structure rather than the bulk rheological resistance. A larger chamfer radius provides a smoother transition between the inlet channel and the working chamber, thereby reducing local separation, vortex formation, and pressure loss. Consequently, although its effect on the overall inlet flow rate was weaker, the chamfer remains beneficial for improving flow uniformity and reducing local energy dissipation.

5.4. Verification of the Optimal Parameter Combination

To gain a comprehensive understanding of how the suction and discharge device operates at its optimal performance level, it is necessary to conduct a simulation analysis of its operational process to observe changes in the volumetric flow rate at the inlet, as well as changes in the pressure and velocity of the grease within the chamber during operation.

5.4.1. Pressure Distribution Under the Optimal Parameter Combination

Figure 16 shows a pressure distribution contour plot of the grease suction phase during the operation of the suction and discharge device. As shown in Figure 16, when grease enters the inlet region of the device, the pressure field distribution is relatively uniform, with no obvious pressure jumps or localized high or low pressure zones; the overall pressure gradient is gentle and reasonable. Unlike the typical condition shown in Figure 13, the pressure transition from the inlet channel to the working chamber is smoother, and the local pressure fluctuation near the inlet–chamber junction is weakened. The pressure contours in Figure 16b–d indicate that the grease can spread more uniformly after entering the chamber, with fewer obvious pressure concentration regions. This suggests that the optimized parameters reduce local pressure loss and improve the stability of grease suction This uniform pressure distribution indicates that the suction and discharge device effectively

balances flow resistance across all regions during the suction process, allowing the grease to diffuse smoothly within the chamber and preventing flow segregation or localized voids caused by pressure concentration. The chamfered design facilitates the thorough and uniform distribution of grease throughout the chamber, thereby ensuring the integrity and consistency of the suction process and providing an optimal initial filling condition for subsequent efficient grease discharge.

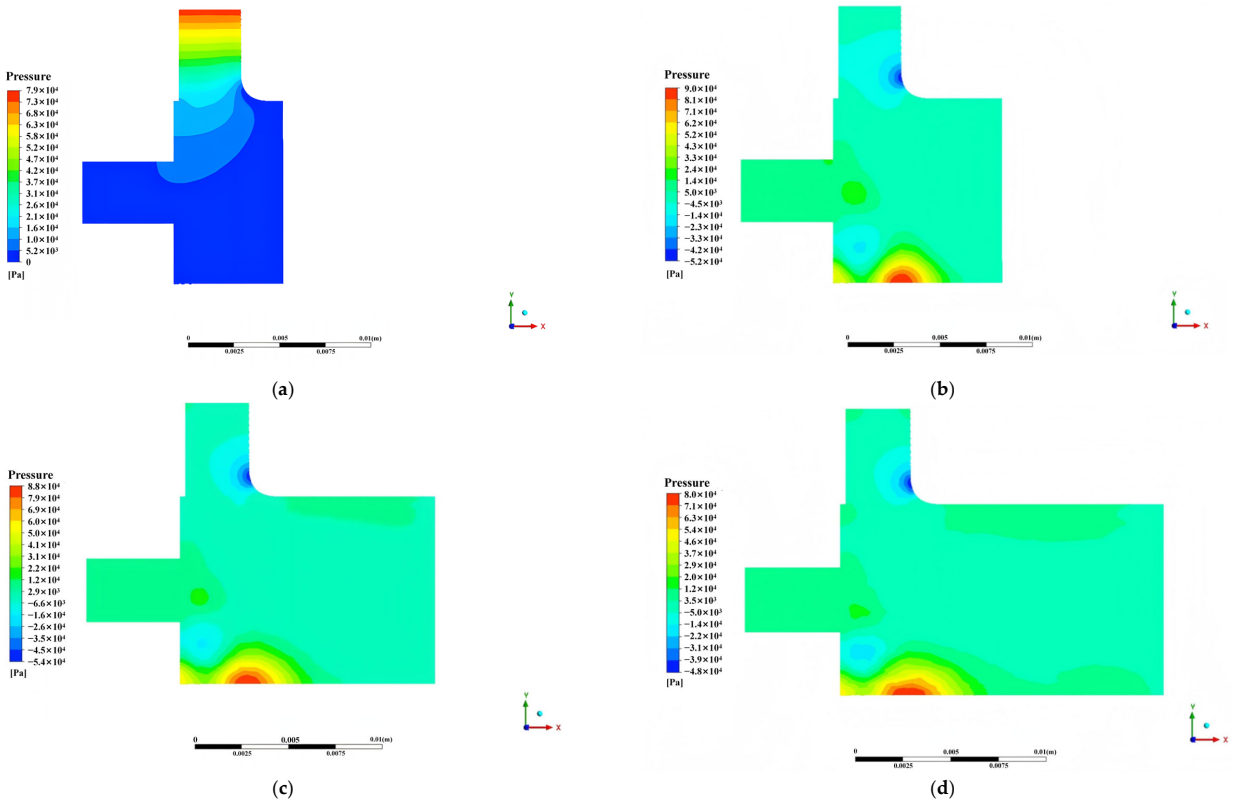


Figure 16. Pressure distribution during the suction stroke under optimal parameter selection. (**a**) 0.001 s; (**b**) 0.012 s; (**c**) 0.024 s; and (**d**) 0.036 s.

5.4.2. Flow Velocity Distribution Under the Optimal Parameter Combination

Figure 17 shows the velocity distribution contour plot of the grease during the suction phase of the suction and discharge device during operation. At the initial stage, as shown in Figure 17a, the high-velocity region is mainly concentrated in the inlet channel. As the suction stroke proceeds, Figure 17b,c show that this high-speed flow enters the working chamber with a smoother transition and a wider distribution range. At the final stage, as shown in Figure 17d, the chamber velocity field becomes more organized and tends toward a stable distribution. Compared with the pre-optimized velocity distribution shown in Figure 14, the optimized structure reduces the abrupt velocity change at the inlet–chamber junction, weakens local stagnation and vortex formation, and improves the continuity of grease filling in the chamber. This indicates that the optimization effectively improves grease distribution, helping to reduce energy loss and localized stagnation. Furthermore, in terms of velocity values, the maximum velocity after optimization increased by 29.2% compared to the pre-optimization design. This significant improvement signifies enhanced grease delivery capacity within the suction and discharge device, enabling a faster filling process with more complete and uniform filling. Overall, higher flow velocities help overcome local flow resistance in the channels and accelerate the diffusion of grease to all areas, thereby ensuring that the suction and discharge device fills quickly and uniformly with grease, improving dispensing efficiency and operational stability.

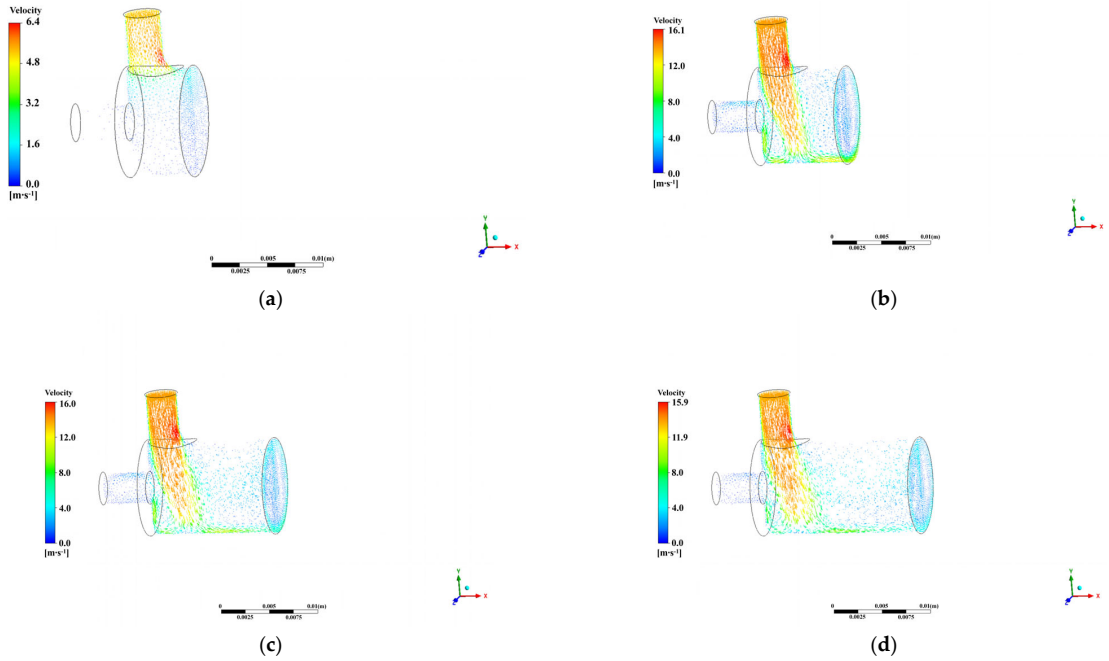


Figure 17. Velocity distribution during the suction stroke under optimal parameter selection. (**a**) 0.001 s; (**b**) 0.012 s; (**c**) 0.024 s; and (**d**) 0.036 s.

5.4.3. Changes in Volumetric Flow Rate

Figure 18 shows the variation in the volumetric flow rate of grease passing through the inlet of the suction and discharge device during the grease suction process. As the procedure progresses, the volumetric flow rate at the inlet gradually increases from 0 to 138.5 mL·s^{-1}, then fluctuates before stabilizing at approximately 131.2 mL·s^{-1}. This trend in volumetric flow rate indicates that, in the early stages of grease suction process, the flow resistance of the grease is low due to a significant vacuum pressure difference, resulting in a rapid increase in volumetric flow rate. As the internal pressure of the suction and discharge device gradually increases, the vacuum difference gradually decreases, and the resistance to grease flow increases, causing the volumetric flow rate to decrease slightly. Ultimately, when the internal and external pressures of the suction and discharge device reach a relatively stable state, the volumetric flow rate also tends to stabilize. This process not only reflects the impact of internal pressure changes on the flow characteristics of the grease but is also crucial for understanding and predicting the performance of the equipment during different operational phases. Monitoring changes in volumetric flow rate allows for the timely detection of internal blockages and other issues, enabling the implementation of appropriate maintenance measures, which helps extend the service life of the turntable bearings.

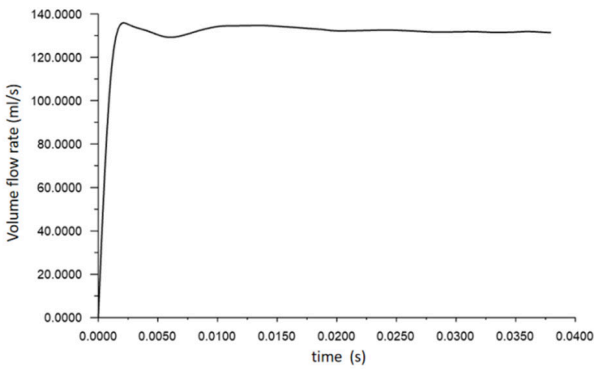


Figure 18. Volumetric flow rate at the inlet.

6. Conclusions and Outlook

6.1. Conclusions

This study investigated the suction performance of a grease suction and discharge device for wind-turbine bearings by combining rheological tests, a Herschel–Bulkley analytical model, CFD simulations, and orthogonal numerical experiments. The main conclusions are as follows:

(1) The tested grease exhibited distinct yield-stress and shear-thinning characteristics within the temperature range of 5–45 °C. Based on the fitted Herschel–Bulkley parameters, an analytical model considering the plug-flow and shear-flow regions was established to describe the relationship between the pressure gradient, grease rheology, and inlet volumetric flow rate.

(2) The analytical and CFD results showed consistent trends, indicating that the inlet volumetric flow rate increased with increasing vacuum level. The differences between the two methods were mainly caused by entrance effects, local expansion, and the transient acceleration of grease during the suction process, which were not considered in the idealized analytical model.

(3) Within the investigated parameter ranges, grease temperature had the strongest effect on suction performance, followed by vacuum level and inlet chamfer radius. The optimal combination was a vacuum level of 0.09 MPa, a grease temperature of 45 °C, and a chamfer radius of 1.7 mm. Under this condition, the maximum grease velocity increased by 29.2%, and the inlet volumetric flow rate stabilized at approximately 131.2 $mL \cdot s^{-1}$. These results provide a reference for the operating-parameter selection and inlet-structure design of grease suction–discharge devices.

6.2. Outlook

The present study adopted an idealized steady analytical model and a single-phase transient CFD model. The results are therefore mainly applicable to systems with continuous grease supply and adequate sealing. Future work will focus on experimental validation, gas–grease two-phase modeling, and the effects of grease thixotropy, aging, contamination.

Author Contributions: Conceptualization, H.P. and M.Z. (Minzhang Zhao); methodology, L.S., B.P. and M.Z. (Mingxuan Zhang); investigation, H.P., L.L. and Y.Z.; writing—original draft preparation, H.P., B.P. and B.H.; writing—review and editing, H.P., Z.Q. and Z.M. All authors have read and agreed to the published version of the manuscript.

Funding: This study was supported by Henan Provincial Key Research and Development Project: "Research and Application of Key Technologies for Intelligent Lubrication in Tunnel Boring Machines", 261111222400. Graduate Student Innovation Ability Enhancement Project at North China University of Water Resources and Electric Power, NCWUYC202617052. Research and Practice Project on Educational and Teaching Reform at North China University of Water Resources and Electric Power, 2026XJGXM033.

Data Availability Statement: The original contributions presented in this study are included in the article. Further inquiries can be directed to the corresponding author.

Conflicts of Interest: Minzhang Zhao and Bingli Huang were employed by Zhengzhou Autol Technology Co., Ltd. Other authors declare no conflict of interest.

References

1. Jinping, L. A state-of-the-art review on wind power converter fault diagnosis. *Energy Rep.* **2022**, *8*, 5341–5369. [CrossRef]
2. Chapman, J.T. Some Aspects of Lubricant Development of Centralised Aerosol Lubricating Systems. *Sci. Lubr.* **1996**, *18*, 23–28.
3. Hart, E.; Mello, E.D.; Dwyer-Joyce, R. Wind turbine main-bearing lubrication-Part 1: An introductory review of elastohydrodynamic lubrication theory. *Wind Energy Sci.* **2022**, *7*, 1021–1042. [CrossRef]

4. Liu, Z.; Zhang, L. A review of failure modes, condition monitoring and fault diagnosis methods for large-scale wind turbine bearings. *Measurement* **2019**, *149*, 107002.
5. Shangguan, J. Design and Experimental Research on Centralized Lubrication and Waste Oil Recovery System for Wind Turbines. *Appl. Sci.* **2023**, *13*, 1873. [CrossRef]
6. Yeong, S.K.; Luckham, P.F.; Tadros, T. Steady flow and viscoelastic properties of lubricating grease containing various thickener concentrations. *J. Colloid Interface Sci.* **2004**, *274*, 285–293. [CrossRef] [PubMed]
7. Cyriac, F.; Lugt, P.M.; Bosman, R. Yield Stress and Low-Temperature Start-Up Torque of Lubricating Greases. *Tribol. Lett.* **2016**, *63*, 6. [CrossRef]
8. Sarkar, C.; Westerberg, L.G.; Höglund, E.; Lundström, T.S. Numerical Simulations of Lubricating Grease Flow in a Rectangular Channel with and without Restrictions. *Tribol. Trans.* **2017**, *61*, 144–156. [CrossRef]
9. Zhang, X.; Chen, F.; Gao, Y.; Wei, C.; Tang, G. Silicone Grease Storage Life Evaluation for Bearings. *Lubr. Eng.* **2020**, *45*, 125–128.
10. Li, R. Effect of static thermal aging on grease soap fiber entanglement and recovery properties. *Lubr. Eng.* **2016**, *93*, 97.
11. Zhao, Q. Research on the relationship between thermal aging of lubricating grease outside the contact area of bearing rolling elements and bearing lubrication failure. *Eng. Fail. Anal.* **2025**, *168*, 109127. [CrossRef]
12. Yusufi, B.K.; Kapelan, Z.; Mehta, D. Advances in modeling the flow of Herschel–Bulkley fluids in pipes: A review. *Phys. Fluids* **2025**, *37*, 021302. [CrossRef]
13. Calusi, B.; Farina, A.; Fusi, L.; Vergori, L. Viscoplastic flows in narrow channels: Herschel–Bulkley model versus its regularizations. *Phys. Fluids* **2025**, *37*, 093101. [CrossRef]
14. Maccioni, L.; Concli, F. Computational Fluid Dynamics Applied to Lubricated Mechanical Components: Review of the Approaches to Simulate Gears, Bearings, and Pumps. *Appl. Sci.* **2020**, *10*, 8810. [CrossRef]
15. Obata, T.; Fujiwara, H.; Itoigawa, F.; Maegawa, S. Effect of Grease Viscosity on Channeling Properties of Ball Bearings. *Lubricants* **2024**, *12*, 13. [CrossRef]
16. Van der Meer, G.H.G.; Van Ostayen, R.A.J. Efficient solution method for the Reynolds equation with Herschel–Bulkley fluids. *Tribol. Int.* **2024**, *204*, 110460.
17. Stosiak, M.; Bury, P.; Karpenko, M. The Influence of Hydraulic Hose Length on Dynamic Pressure Waveforms Including Wave Phenomena. *Sci. Rep.* **2025**, *15*, 31548. [CrossRef] [PubMed]
18. Urbanowicz, K.; Bergant, A.; Stosiak, M.; Deptuła, A.; Karpenko, M. Navier–Stokes Solutions for Accelerating Pipe Flow—A Review of Analytical Models. *Energies* **2023**, *16*, 1407. [CrossRef]
19. Li, F. Waste Oil Recycling Purification and Reuse System. CN211799281U, 30 October 2020.
20. Chen, X. A study on grease collection in wind turbine pitch bearings drainage. *Wind Energy* **2019**, *74*, 77.
21. Quan, H. Centralized Recycling of Waste Grease and Automatic Cleaning System of Wear Chips for Wind Power Bearings. CN216045031U, 15 March 2022.
22. Si, K. An electric Grease Suction and Discharge Device and Waste Grease Recovery System. CN212719140U, 23 March 2021.
23. Suo, J. A Grease Suction and Discharge Device and a Bearing Waste Grease Discharge Device. CN118462724A, 13 August 2024.
24. Jiang, Z.; Huang, X. A new method for contact characteristic analysis of the tapered roller bearing in wind turbine main shaft. *Eng. Fail. Anal.* **2022**, *141*, 10672. [CrossRef]
25. Behnke, K. Exploring limiting factors of wear in pitch bearings of wind turbines with real-scale tests. *Wind Energy Sci.* **2023**, *8*, 289–301. [CrossRef]
26. Stammler, M. Short-Term Influence of Water Ingress on Wear in Pitch Bearings of Wind Turbines. *Lubricants* **2024**, *12*, 310. [CrossRef]
27. Zhao, P. Automatic Removal and Centralized Recycling System for Waste Grease of Wind Turbine Bearings. In Proceedings of the 8th China (Shanghai) International Wind Energy Exhibition and Conference, Shanghai, China, 8–10 April 2014; Volume 1, pp. 1–5.
28. Wang, B. Research on automatic centralized waste grease collection system for wind turbine bearings. *Wind Power* **2016**, *32*, 35.
29. Yan, F.; Wang, Z.; Du, Y.; Su, S.; Zheng, Y.; Li, Q. Research on rheological and flow behavior of lubricating grease in extremely cold weather. *Ind. Lubr. Tribol.* **2017**, *69*, 1066–1073. [CrossRef]
30. Lan, W.; Wu, A. The Equation of Flow in Pipes for Non-Newtonian Fluids and Its Approximate Solutions. *J. Harbin Inst. Technol.* **2020**, *52*, 140–146.
31. Lan, W.; Wu, A. Derivation and Experimental Validation of General Equations for Flow in Pipelines. *J. Huazhong Univ. Sci. Technol. (Nat. Sci. Ed.)* **2019**, *47*, 61–65.
32. Wang, J.; Zhang, H.; Hu, W.; Li, J. Tribological Properties and Lubrication Mechanism of Nickel Nanoparticles as an Additive in Lithium Grease. *Nanomaterials* **2022**, *12*, 2287. [CrossRef] [PubMed]
33. Xu, L. Study on Preparation of Lube Base Oil from the Desert Amygdaluspcdunculata Pall Oil. Master's Thesis, Northwest University, Xi'an, China, 2014.
34. Li, H.; Chu, Y.; Dong, L.; Wang, J.; Zhao, M. A Study on Universal Extreme-Pressure Additive Packages for Lithium-Based Greases. *Lubr. Seal.* **2025**, *50*, 199–204.

35. Wang, Y.; Gao, X.; Lin, J.; Zhang, P. Rheological and Frictional Properties of Lithium Complex Grease with Graphene Additives. *Lubricants* **2022**, *10*, 57. [CrossRef]
36. *DIN 51810-2:2017*; Testing of Lubricants—Testing Rheological Properties of Lubricating Greases—Part 2: Determination of Flow Point Using an Oscillatory Rheometer with a Parallel-Plate Measuring System. DIN Deutsches Institut für Normung e.V.: Berlin, Germany, 2017.
37. Karpenko, M. Aircraft hydraulic drive energy losses and operation delay associated with the pipeline and fitting connections. *Aviation* **2024**, *28*, 1–8. [CrossRef]
38. Zhao, P. Wind Turbine Bearing Waste Grease Automatic Removal and Centralized Recycling System. *Wind Energy Ind.* **2013**, *71*, 74.
39. Hisam, M.W.; Dar, A.A.; Elrasheed, M.O.; Khan, M.S.; Gera, R.; Azad, I. The Versatility of the Taguchi Method: Optimizing Experiments Across Diverse Disciplines. *J. Stat. Theory Appl.* **2024**, *23*, 365–389. [CrossRef]
40. Nagare, P.; Kudal, H. A Taguchi Approach on Influence of Graphite as an Anti-Wear Additive on the Performance of Lithium Grease. *Procedia Manuf.* **2018**, *20*, 487–492. [CrossRef]

Disclaimer/Publisher's Note: The statements, opinions and data contained in all publications are solely those of the individual author(s) and contributor(s) and not of MDPI and/or the editor(s). MDPI and/or the editor(s) disclaim responsibility for any injury to people or property resulting from any ideas, methods, instructions or products referred to in the content.